Helical waves in easy-plane antiferromagnets

Yuriy G. Semenov, Xi-Lai Li, Xinyi Xu, and Ki Wook Kim

Phys. Rev. B **96**, 224432 — Published 28 December 2017

DOI: 10.1103/PhysRevB.96.224432

Helical waves in easy-plane antiferromagnets

Yuriy G. Semenov,[1] Xi-Lai Li,[1] Xinyi Xu,[1] and Ki Wook Kim[1,2]

[1]*Department of Electrical and Computer Engineering, North Carolina State University, Raleigh, NC 27695, USA*

[2]*Department of Physics, North Carolina State University, Raleigh, NC 27695, USA*[*]

Abstract

Effective spin torques can generate the Néel vector oscillations in the antiferromagnets (AFMs). Here, it is theoretically shown that these torques applied at one end of a normal AFM strip can excite a helical type of spin waves in the strip whose properties are drastically different from the characteristic spin waves. The analysis based on both a Néel vector dynamical equation and the micro-magnetic simulation identifies the direction of magnetic anisotropy and the damping factor as the two key parameters determining the dynamics. The helical wave propagation requires the hard axis of the easy-plane AFM to be aligned with the traveling direction, while the damping limits its spatial extent. If the damping is neglected, the calculation leads to uniform periodic domain wall structure. On the other hand, finite damping decelerates the helical wave rotation around the hard axis causing ultimately stoppage of its propagation along the strip. With the group velocity staying close to spin-wave velocity at the wave front, the wave length becomes correspondingly longer away from the excitation point. In a sufficiently short strip, a steady-state oscillation can be established whose frequency is controlled by the waveguide length as well as the excitation energy or torque.

PACS numbers: 75.75.-c, 75.78.Jp, 75.85.+t, 85.70.Ay

[*] kwk@ncsu.edu

I. INTRODUCTION

Helimagnets and helical structures in ferromagnets (FMs) or antiferromagnets (AFMs) are the characteristic states found usually in rather complex magnetic crystals. The origin of magnetic helicity stems from the interplay of several competing interactions such as the exchange interaction, crystalline anisotropy, and Dzyaloshinskii-Moriya interaction. A thermodynamically stable, inhomogeneous distribution of the magnetic moments in the form of helical waves (HWs) has been studied extensively as can be found in the literature (see Ref. [1] and the references therein). A particularly interesting issue is the spatial structure of these HWs in the presence of external parameters such as, for instance, an applied magnetic field [2]. It is evident that controlled generation and manipulation of HWs in more common magnets can offer additional prospects in the pursuit of magnetic materials and their applications.

The desired magnetization dynamics may be achieved by taking advantage of the effective spin torques that have shown to produce oscillations of order parameters in FMs or AFMs via the current-driven or even currentless mechanisms [3–10]. Of the two classes of magnetic materials, AFMs in particular have received much attention recently due to the fast sublattice magnetization dynamics (and those of the Néel vector) as well as their insensitivity to the spurious magnetic fields. These distinctive features rely on the absence or sufficient suppression of macroscopic angular momentum that allows the Néel vector rotation to continue even after the applied torque ceases [10, 11]. Consequently, persistent oscillations up to THz frequencies can be generated [7–10]. Applying a spin torque at one end of a long AFM strip would undoubtedly alter the state of magnetic equilibrium in a certain manner specific to the torque strength and parameters of the structure.

In this paper, it is theoretically demonstrated that a long easy-plane AFM strip can serve as a waveguide transferring the Néel vector rotation in the form of HWs. The specific structures under consideration are shown in Fig. 1, where an effective torque is employed only at one end of the strip. In contrast to helimagnets, the spin torque establishes the HWs as the final outcome of transient processes. As such, the resulting Néel vector dynamics exhibit a strong dependence on the nature of the applied torque (e.g., anti-damping vs. field-like). The analysis takes advantage of a simplified model that is developed to describe HW transient dynamics based on the spatial and temporal progression of the Néel vector

chiral phase along the AFM hard axis. Micro-magnetic simulations are also applied for comparison as well as to elucidate the steady-state characteristics in the waveguides of finite lengths. A brief discussion on the detection of HWs is provided toward the end.

II. EQUATIONS OF MOTION

An approach that can conveniently describe the AFM dynamics results from the symmetry analysis and subsequent formulation of the corresponding Lagrangian in terms of the Néel vector ($\mathbf{L}$) as well as its spatial and temporal derivatives [12]. This description supposes the dominant exchange interaction between magnetic sublattices resulting in the relatively small AFM magnetization $\mathbf{M}$ (i.e., $|\mathbf{L}| \equiv L \gg |\mathbf{M}|$). The former is commonly represented by a strong exchange field H_{ex} ($\sim$ MOe) aligning the sublattice magnetizations in opposite directions. Consequently, the length of the Néel vector (L) can be treated approximately as an integral of the motion. This simplification reduces the relevant vector variables for each sublattice magnetization to a single normalized quantity $\mathbf{n} \equiv \mathbf{L}/L = (n_x, n_y, n_z)$. In the case of a sufficiently small waveguide width Δ (i.e., $\Delta \ll v_m/\omega$, where ω is the typical frequency of the Néel vector rotation and v_m the magnon velocity), the transversal variation in the Néel vector can become negligible. As such, the only spatial variable z along the AFM waveguide and time t determine the Néel vector [thus, $\mathbf{n}(z,t)$], which in turn uniquely defines the Lagrangian [12–15]

$$\mathfrak{L} = \frac{L^2}{2\omega_{ex}^2}[\dot{\mathbf{n}}_{(t)}^2 - v_m^2 \dot{\mathbf{n}}_{(z)}^2] - \frac{L^2}{\omega_{ex}^2}[\dot{\mathbf{n}}_{(t)} \times \mathbf{n}]\cdot\gamma\mathbf{H} + \frac{L^2}{2\omega_{ex}^2}(\mathbf{n}\times\gamma\mathbf{H})^2 - W(\mathbf{n}), \tag{1}$$

where $\omega_{ex}^2 = \gamma^2 H_{ex} L$, $\dot{\mathbf{n}}_{(i)} \equiv \partial\mathbf{n}/\partial i$ ($i = z,\, t$), γ is the gyromagnetic ratio, and $\mathbf{H}$ denotes the magnetic field of external and/or internal origin. More specifically, the first two terms in the square brackets represent the density of kinetic energy and the inhomogeneous exchange interaction, respectively, while the next two are for the contributions of the dynamic and static susceptibility to the AFM magnetic energy in the presence of a magnetic field $\mathbf{H}$ [14]. Lastly, $W(\mathbf{n})$ describes the density of anisotropy energy. It is interesting to note that, at $v_m = 0$ and $|\mathbf{H}| = 0$, the expression given in Eq. (1) mimics the Lagrangian for a pendulum with the "kinetic" energy (i.e., the $\dot{\mathbf{n}}_{(t)}^2$ term) and the "potential" energy $W(\mathbf{n})$. Likewise, a finite magnetic field corresponds to the external forces. In an AFM with the easy x-y plane

and the hard z axis, the density of anisotropy energy can be expressed as

$$W(\mathbf{n}) = \frac{1}{2} K n_z^2, \tag{2}$$

where K (> 0) represents the strength of magnetic anisotropy along the hard z axis.

As noted above, the present analysis is focused on the excitation of Néel vector rotation and subsequent propagation along the AFM waveguide. The most reliable approaches adopted thus far to trigger the Néel vector oscillations have been based on either the spin transfer torque [9, 10, 16] or the spin-orbit torque [6–8]. Both of these mechanisms can be represented via the electron spin polarization $\mathbf{P}$ (with $\mathbf{p} \equiv \mathbf{P}/\left|\mathbf{P}\right|$) of the spin current flowing into the AFM, which results in an anti-damping torque $\eta \mathbf{n} \times (\mathbf{n} \times \mathbf{p})$. Here, the parameter η reflects the efficiency of the process [7]. Friction proportional to the angular velocity of the Néel vector also arises against the anti-damping torque, which hinders excitation of the oscillations. Thus the energy loss accompanies the Néel vector precession. Combined with the torque-induced energy gain, the dissipation function can then be expressed as [13]

$$\mathfrak{R} = R \dot{\mathbf{n}}_{(t)}^2 + \eta (\mathbf{n} \times \mathbf{p}) \cdot \dot{\mathbf{n}}_{(t)}, \tag{3}$$

where $R = \delta_r L^2 / 4\omega_{ex}^2$ with δ_r from the width of AFM resonance. A constant value is used for R in the ensuing discussion even with a large deviation of the Néel vector from equilibrium. In the case of a field-like torque, the effect on the excitation does not require a separate description as it can be addressed by simply adding an appropriate contribution to $\mathbf{H}$. The corresponding friction is naturally accounted for by the first term in Eq. (3).

Taking into account the unimodularity $|\mathbf{n}| = 1$, the Euler-Lagrange equation reads

$$\mathbf{n} \times \left[\frac{\partial}{\partial t} \frac{\partial \mathfrak{L}}{\partial \dot{\mathbf{n}}_{(t)}} + \frac{\partial}{\partial z} \frac{\partial \mathfrak{L}}{\partial \dot{\mathbf{n}}_{(z)}} - \frac{\partial \mathfrak{L}}{\partial \mathbf{n}} + \frac{\partial \mathfrak{R}}{\partial \dot{\mathbf{n}}_{(t)}} \right] = 0. \tag{4}$$

Substitution of Eqs. (1)−(3) into Eq. (4) yields a set of equations for the components of vector $\mathbf{n}(z,t)$. Formulation with dimensionless variables $w(\mathbf{n}) = W(\mathbf{n})/K$, $\mathbf{h} = \gamma \mathbf{H}/\omega_r$, $t \to \omega_r t$, $z \to kz = \omega_r z / v_m$ explicitly transforms Eq. (4) to a partial differential equation (PDE)

$$\mathbf{n} \times \left[\ddot{\mathbf{n}}_{(tt)} - \ddot{\mathbf{n}}_{(zz)} + 2(\dot{\mathbf{n}}_{(t)} \times \mathbf{h}) - (\mathbf{n} \times \dot{\mathbf{h}}_{(t)}) + \mathbf{h}(\mathbf{n} \cdot \mathbf{h}) + \frac{1}{4} \frac{\partial}{\partial \mathbf{n}} w(\mathbf{n}) + 2\lambda \dot{\mathbf{n}}_{(t)} + \sigma(\mathbf{n} \times \mathbf{p}) \right] = 0, \tag{5}$$

where $\omega_r = \gamma\sqrt{2H_{ex}H_{an}}$ for the zero-field AFM resonance frequency, $H_{an} = K/\frac{1}{2}L$ for the effective anisotropy field, $\lambda = \delta_r/\omega_r$ $(= R\omega_r/K)$ for characteristic damping, and

$$\sigma(z,t) = \frac{\eta(z,t)}{L^2}\frac{H_{ex}}{2H_{an}}. \tag{6}$$

Further simplification can be done if one takes into account that the system maintains the axial symmetry provided that the spin current mediates a spin torque collinear to the hard z-axis. As shown in Fig. 1(a), spin polarization $\mathbf{p}$ of the injected spin current is chosen to match the hard axis of the AFM layer. This configuration confines the Néel vector within the energetically favorable x-y plane. The cylindrical symmetry permits us to parameterize the Néel vector as $\mathbf{n}(z,t) \to \mathbf{n}(\vartheta,\varphi,t) = (\sin\vartheta\cos\varphi, \sin\vartheta\sin\varphi, \cos\vartheta)$ in terms of the polar $\vartheta = \vartheta(z,t)$ and azimuthal $\varphi = \varphi(z,t)$ angles. Substituting $\mathbf{n}(\vartheta,\varphi,t)$ into Eq. (5) separates the variables $\vartheta(z,t)$ and $\varphi(z,t)$ so that the polar angle $\vartheta(z,t)$ is essentially a time-space independent constant $\pi/2$. Then, the final expression for the remaining variable $\varphi = \varphi(z,t)$ is given as

$$\frac{\partial^2\varphi}{\partial t^2} - \frac{\partial^2\varphi}{\partial z^2} + 2\lambda\frac{\partial\varphi}{\partial t} = \Phi(z,t), \tag{7}$$

where $\Phi(z,t)$=$\sigma(z,t) - \dot{h}_{(t)}(z,t)$. The first term $\sigma(z,t)$ represents the contribution of the anti-damping torque, while the field-like torque $\dot{h}_{(t)}(z,t)$ is introduced via the time derivative of the effective field $\mathbf{h}$. Note that the derivation of Eq. (7) is predicated on local invariance of the Lagrangian with respect to the Néel vector rotation around the hard axis (which is collinear to the applied spin torque). Thus, the formulation would similarly be applicable if both the torque and the hard axis are along the normal y-direction.

III. SOLUTIONS OF BASIC EQUATION

It is rather surprising that the non-linear equations of AFM dynamics for the Néel vector components are reduced to a linear equation for the azimuthal angle in a one-dimensional configuration space. This inhomogeneous, second-order PDE needs to be solved for time $t > 0$ with the initial conditions for the Néel vector and its time derivative. In the present analysis, it is assumed that the Néel vector in the AFM layer is initially aligned along the x axis and stationary; i.e., $\mathbf{n}(z, t = 0) = (1, 0, 0)$ and $\dot{\mathbf{n}}_{(t)}(z, t = 0) = (0, 0, 0)$. These conditions appear in the angular variables as

$$\varphi(z,t)|_{t=0} = \dot{\varphi}_{(t)}(z,t)|_{t=0} = 0. \tag{8}$$

Unlike the bi-axial cases studied previously [8–10, 16], the Néel vector in an easy-plane AFM nanoparticle [i.e., Eq. (7)] starts to rotate at any torque with the divergent frequency of

$$\omega_p = \frac{T_q}{2\lambda}\left(1 - e^{-2\lambda t}\right), \tag{9}$$

reaching the steady state in time $t \gg 1/2\lambda$.

To examine the effect of long waveguides, Eq. (7) is reduced to the inhomogeneous relativistic Klein-Gordon equation by using the substitution $\varphi(z,t) = u(z,t)e^{-\lambda t}$:

$$\ddot{u}_{(tt)} - \ddot{u}_{(xx)} + \lambda^2 u = e^{\lambda t}\Phi(z,t). \tag{10}$$

In doing so, it is chosen not to correct the boundary conditions to avoid the inessential complications. While this approximation assumes no reflected wave from the far end of the waveguide, it is expected to remain valid for a sufficiently long channel considering that the damping can significantly reduce the boundary effect. The above Klein-Gordon equation with the given initial conditions [Eq. (8)] can be approached via integral transformation [17]. The resulting solution can be expressed in the form

$$\varphi(z,t) = \frac{1}{2}\int_0^t \int_{z-s}^{z+s} \Phi(\zeta, t-s)e^{-\lambda s} J_0\left(-\lambda\sqrt{s^2-(z-\zeta)^2}\right) d\zeta ds, \tag{11}$$

where $J_0(x)$ is a Bessel function. This integral presentation can be numerically evaluated for arbitrary disturbances, $\Phi(z,t)$, applied along the AFM strip (see Fig. 1 for the set-up). The excitation torque may be represented conventionally in a multiplicative form

$$\Phi(z,t) = T_q f_z(z) g_t(t), \tag{12}$$

where $f_z(z)$ determines the location of the applied torque, $g_t(t)$ the time dependence, and T_q the amplitude.

Consider the torque localized around the origin $z = 0$, as illustrated in Fig. 1, in a space scale much shorter than the wave length. A subsequent approximation of $f_z(z) = \delta(z)$ reduces Eq. (11) to a more manageable expression

$$\varphi(z,t) = \frac{T_q}{2}\int_0^t \chi(z,s) g_t(t-s) e^{-\lambda s} J_0\left(\lambda\sqrt{s^2-z^2}\right) ds, \tag{13}$$

where

$$\chi(z,s) = \frac{sgn(s+z) + sgn(s-z)}{2}. \tag{14}$$

For a semi-infinite strip (i.e., $z > 0$), the torque efficiency is doubled as is the case in the rest of the discussion. Equation (13) describes evolution of the Néel vector $\mathbf{n} = [\cos\varphi(z,t), \sin\varphi(z,t), 0]$ as well as the HW "group velocity" $v_g = -\dot{\varphi}_{(t)}(z,t)/\dot{\varphi}_{(z)}(z,t)$ and the rotation frequency $\omega_p(z,t) = \dot{\varphi}_{(t)}(z,t)$ along the waveguide. Equations (13) and (14) explicitly reveal the retardation between the excitation and the response (of $t = z$ or $t = z/v_m$ in dimensional units).

IV. TRANSIENT AND STEADY-STATE DYNAMICS OF HELICAL WAVES

We start the analysis of Eq. (13) with the dissipationless case $\lambda = 0$. It can be seen in Fig. 2(a) that Eq. (13) describes the self-similar wave train with variable $\xi = t - |z|$ (in conventional units $\xi = \omega_r t - k|z|$) provided that once applied at $t = 0$ the torque remains constant T_q [i.e., $g_t(t) = \theta(t)$ is the Heaviside step function]. Thus Eq. (13) reduces to $\varphi(z,t) = T_q \xi \theta(\xi)$. The results clearly amount to the desired generation of HWs in an AFM strip which can travel over a long distance without dissipation. In this case, the speed of the Néel vector rotation is proportional to the strength of the applied torque [i.e., $\omega_p(z,t) = T_q \omega_r$], whereas the group velocity v_g $(= \omega_r/k)$ corresponds to the magnon velocity v_m independent of the external forces. While the necessary constant torque (more accurately, in a step-function form) can be realized in theory by both the anti-damping and field-like terms, the latter requires an effective field linearly increasing in time. On the other hand, the anti-damping simply requires to turn on a constant excitation current or bias. As such, the discussion in the present section focuses on this mechanism, specifically the spin-orbit torque in the physical system shown in Fig. 1(a).

Once the dissipation is accounted for, the HW dynamics for the step-function torque change rather significantly from the simple picture as shown in Fig. 2(b). The rotation around the hard z-axis [i.e., $\omega_p(z,t)$] progressively slows down away from the excitation point, while the group velocity v_g maintains close to v_m. Accordingly, the wavelength is shown to elongate gradually as $\Lambda = 2\pi v_g/\omega_p(z,t)$. However, the asymptotic behavior of $\omega_p(z,t)$ at $t \to \infty$ is not so evident in contrast to the stationary oscillations excited in small AFM particles [Eq. (9)]. In fact, it is found that the oscillations stop moving spatially and temporally (or become "frozen") with $t \to \infty$ and an aperiodic static Néel vector pattern is

established [Fig. 2(c)], resembling a stable helimagnet structure:

$$\varphi(z,t) \underset{t\to\infty}{\to} \frac{T_q}{\sqrt{2}\lambda} e^{-\sqrt{2}\lambda z}. \tag{15}$$

The total number of static windings around the z axis can be estimated as $N_{\rm HW} = T_q/\sqrt{8}\pi\lambda$, while the distance ΔL needed for the first 360° rotation of the pattern is (in dimensional units)

$$\Delta L = \frac{v_m}{\sqrt{2}\lambda\omega_r} \ln(2N_{\rm HW}). \tag{16}$$

In a dielectric AFM, this length can be as large as a few μm. To achieve at least one reversal of the Néel vector (i.e., one full winding or twisting), the spin torque must exceed a critical value $\sqrt{2}\pi\lambda$. An increase of the torque slowly extends the HW's reach along the AFM strip as a logarithmic function. The established helical structure is maintained only during the presence of the excitation torque. As soon as it is turned off, the domain wall-like pattern starts to unwind and the AFM returns to the equilibrium state $\varphi(z,t) = 0$.

For further analysis, it is illustrative to compare the rotational speed $\omega_p(z,t)$ and the group velocity $v_g(z,t)$ at the origin and at the wave front; thus at $z = 0$ and $z = t$. The results are shown in Fig. 3. In the trivial case of $\lambda = 0$, uniform oscillations persist with no change observed in the HW characteristics. In other words, both ω_p and v_g remain constant spatially and temporally [see, for instance, lines 3 in Fig. 3(a,b)]. When non-zero damping is considered, the rotational speed at both ends tends to zero as $t \to \infty$ for $\omega_p(z = 0, t) = T_q e^{-\lambda t} J_0(\lambda t)$ and $\omega_p(z = t, t) = T_q e^{-\lambda t}$ [curves 1 and 2, respectively, in Fig 3(a)]. This is also consistent with the physical picture emerged from Fig. 2. On the other hand, the group velocity behaves differently. While it decreases exponentially with time at the excitation point, the front of the HWs continues to move at the magnon velocity [$v_g(z = 0, t) = e^{-\lambda t} J_0(\lambda t)$ and $v_g(z = t, t) = 1$; curve 1 and line 2, respectively, in Fig. 3(b)]. An additional point of interest is a damped pendulum-like feature that is apparent from the evolution of the Néel vector at/around $z = 0$. As illustrated, relaxation to the stationary state starts with the deceleration of ω_p and v_g. Then, this damping overshoots to the region with negative values, followed by a gradual decay to zero (see $\omega_r t = 25 - 50$ in the insets to Fig. 3). The negative values in ω_p and v_g indicate that the Néel vector rotation reverses its direction or chirality before stopping its movement finally.

At the first glance, the freeze in the HWs appears incompatible with the steady torque particularly since the friction also diminishes when the Néel vector texture rotates slowly

[see the first term in Eq. (3)]. The seeming contradiction is resolved if one takes into account that the inhomogeneous exchange interaction in the twisted texture exerts a counteraction to the externally applied torque. The shorter the wavelengths at the excitation point are, the stronger the reaction to the torque becomes which finally stops the HWs from developing. Thus, the energy from the current-induced steady torque is expended before it can excite additional oscillations in the long AFM strip. In the case of a sufficiently short waveguide length, the torque is not fully compensated and a steady-state oscillation can be excited through the entire AFM strip with the Néel vector texture similar to that in Fig. 2(b). Apparently the coherent Néel vector rotation distributes the friction and dissipation evenly along the waveguide. For a given torque at the excitation point, the rotational speed in the steady state shows an inverse dependence on the waveguide length L. It is also affected by the size of the excitation area L_0. Considering that Eq. (9) for the nanoparticles corresponds to the condition of $L_0 = L$, the frequency for the partial overlap between L and L_0 may scale to

$$\omega_p(z,t) \underset{t\to\infty}{\to} \omega_r \frac{T_q}{2\lambda}\frac{L_0}{L}; L_0 < z < L. \tag{17}$$

This simple estimate shows a good agreement with the micro-magnetic simulations provided in Fig. 4. The numerical results also reveal that transition to the steady-state oscillation involves multiple reflections of the HWs at the channel edges.

Actual realization of the desired structure [i.e., Fig. 1(a)] may be achieved by taking advantage of room-temperature easy-plane AFMs such as FeF_3 and α-F_2O_3 in combination with a heavy metal injector made of Pt or Ta. A typical threshold current density for the Néel vector rotation is expected to be of the order of 10^8 A/cm^2 judging from the recent experimental data obtained in the bi-axial NiO-Pt system [8]. Despite the differences in the AFM properties (i.e., easy-plane vs. bi-axial anisotropy), the underlaying physical mechanism of spin-orbit torque appears comparable in the two systems.

V. BEYOND HELICAL WAVE EXCITATION

While the desired excitation of HWs can be achieved by the anti-damping torque as described above, it is also instructive to examine the effect of a field-like contribution on the Néel vector dynamics. For this, a scheme based on electrical spin pumping is considered in a spin-capacitor structure [see Fig. 1(b)] in place of the heavy metal based spin current injector.

The basic mechanism relies on the net electron spin polarization induced in the AFM through spin-filtered injection/depletion, subsequently mediating an exchange field and thus a field-like torque (i.e., its time derivative) to the constituent sublattice magnetizations [18]. The dynamical response is modeled by adopting, as a typical example for the effective field, an asymmetrical pulse

$$h(t) = h_0(1 - e^{-t/dt})e^{-t/T_1} \tag{18}$$

with a fast rise ($\sim dt$; the circuit RC time) and a slow fall ($\sim T_1$; the electron spin relaxation time) in the course of a longer pulse duration [18]. The results illustrate that the applied field-like torque pushes a local disturbance of Néel vector with the velocity $v_g \simeq v_m$ along the waveguide (Fig. 5). The disturbance quickly relaxes in a distance comparable to the wavelength of the corresponding HW and does not form any wave-like pattern. Evidently the field-like torque is not conducive for HW excitation, at least not with the assumed form of the effective field.

The generated space-time structure of the Néel vector can be detected by using the magnetoresistance effect. In the case of a dielectric AFM (which is preferred due to the weak damping and the potentially low excitation current with no shunting), one can use a tunneling configuration between the two FM contacts placed at the location of interest. One may also take advantage of conductance anisotropy induced in an adjacent conductor with a strong spin-orbit coupling [19]. If, on the other hand, a metallic material is used, the in-plane conductance of the AFM layer may provide the desired knowledge on the twisted magnetic structure (e.g., the number twists or domain walls) analogous to the non-collinear magnetoresistance for magnetic skrymions [20].

VI. SUMMARY

The spin torque applied locally to one end of an easy-plane AFM strip is shown to excite a Néel vector rotation that can propagate over a long distance in the form of HWs. They move along the magnetic waveguide with the ultimate magnon velocity, while the wavelength progressively becomes longer at the wave front due to the effective friction. In a long strip, this transient dynamics relax to a static Néel vector texture over a finite portion under a constant torque. Once the torque is withdrawn, the spring-like texture unwinds and returns to the initial homogeneous AFM state. If the AFM strip is sufficiently short, on the

other hand, a steady-state aperiodic wave pattern is achieved whose rotation frequency is inversely proportional to the length. The typical time scale of the transient processes with HW formation is around tens of ps. This and other striking HW manifestations including controllable wavelength and frequency as well as a large amplitude may offer an intriguing opportunity in the emerging AFM-based spintronics [21, 22].

ACKNOWLEDGMENTS

This work was supported, in part, by the US Army Research Office (W911NF-16-1-0472) and FAME (one of six centers of STARnet, a SRC program sponsored by MARCO and DARPA).

[1] A. L. Felcy, M. M. Latha, and C. C. Vasanthi, Physica B **499**, 49 (2016).

[2] V. Laliena, J. Campo, and Y. Kousaka, Phys. Rev. B **95**, 224410 (2017).

[3] A. Matos-Abiague and R. L. Rodríguez-Suárez, Phys. Rev. B **80**, 094424 (2009).

[4] J. Železný, H. Gao, A. Manchon, F. Freimuth, Y. Mokrousov, J. Zemen, J. Mašek, J. Sinova, and T. Jungwirth, Phys. Rev. B **95**, 014403 (2017).

[5] K. M. D. Hals, Ya. Tserkovnyak, and A. Brataas, Phys. Rev. Lett. **106**, 107206 (2011).

[6] R. Cheng, J. Xiao, Q. Niu, and A. Brataas, Phys. Rev. Lett. **113**, 057601 (2014).

[7] T. Shiino, S.-H. Oh, P. M. Haney, S.-W. Lee, G. Go, B.-G. Park, and K.-J. Lee, Phys. Rev. Lett. **117**, 087203 (2016).

[8] R. Khymyn, I. Lisenkov, V. Tiberkevich, B. A. Ivanov, and A. Slavin, Sci. Rep. **7**, 43705 (2017).

[9] E. V. Gomonay and V. M. Loktev, Phys. Rev. B **81**, 144427 (2010).

[10] R. Cheng, M. W. Daniels, J.-G. Zhu, and D. Xiao, Phys. Rev. B **91**, 064423 (2015).

[11] Y. G. Semenov, X.-L. Li and K. W. Kim, Phys. Rev. B **95**, 014434 (2017).

[12] E. A. Turov, A. V. Kolchanov, M. I. Kurkin, I. F. Mirsaev, and V. V. Nikolaev, *Symmetry and physical properties of antiferromagnetics* (Cambridge International Science Publishing, Cambridge, United Kingdom, 2009), Chap. 11.

[13] E. V. Gomonay and V. M. Loktev, Low Temp. Phys. **40**, 17 (2014).

[14] A. F. Andreev and V. I. Marchenko, Sov. Phys. Usp. **23**, 21 (1980).

[15] B. A. Ivanov, Low Temp. Phys. **31**, 635 (2005).

[16] A. S. Núñez, R. A. Duine, P. Haney, and A. H. MacDonald, Phys. Rev. B **73**, 214426 (2006).

[17] A. N. Tikhonov and A. A. Samarskii, *Equations of mathematical physics* (Dover, New York, 2011), Chap. II.

[18] Y. G. Semenov and K. W. Kim, Appl. Phys. Lett. **110**, 192405 (2017).

[19] X. Marti, I. Fina, and T. Jungwirth, IEEE Trans. Magn. **51**,2900104 (2015).

[20] A. Fert, N. Reyen, and V. Cros, Nat. Rev. Mater. **1**, 17031 (2017).

[21] T. Jungwirth, X. Marti, P. Wadley, and J. Wunderlich, Nat. Nanotechnol. **11**, 231 (2016).

[22] O. Gomonay, T. Jungwirth, and J. Sinova, Phys. Status Solidi RRL **11**, 1700022 (2017).

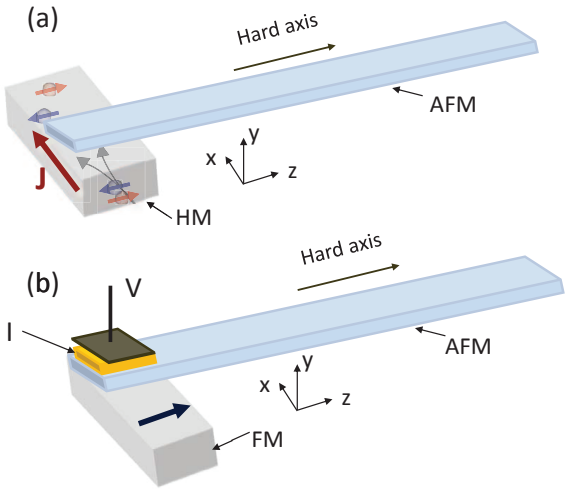

FIG. 1. Schematic illustration of the structures under consideration. (a) An electrical current J through the heavy metal (HM) layer induces the *anti-damping* spin-orbit torque in the adjacent AFM. The arrows show the spin separation due to the spin-Hall effect. (b) Net electron spin in the AFM polarized along the FM magnetization (thick black arrow) generates the *field-like* spin-pumping torque. Under an applied bias, electrons spin-filtered by the FM gather near the AFM interface with the insulating layer (I), providing the effective field. In both (a) and (b), the torque is applied parallel to the AFM hard axis along the strip.

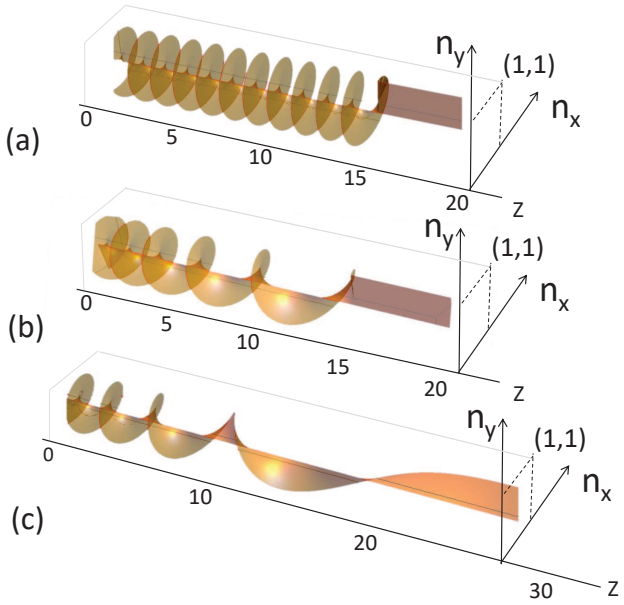

FIG. 2. Snapshots of Néel vector texture $\mathbf{n} = [n_x(z,t), n_y(z,t), 0]$ in the AFM strip under a constant spin torque of T_q=5 at (a,b) instant t=15 and (c) $t \to \infty$. The damping is neglected in (a), while it is set at λ=0.1 for (b,c). Dimensionless units are used.

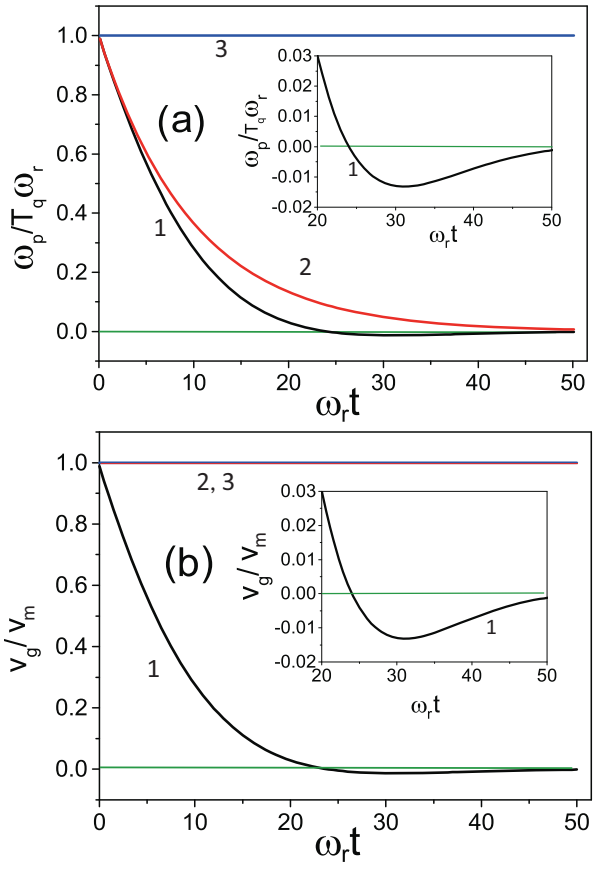

FIG. 3. Temporal dependence of (a) HW rotation frequency $\omega_p(z,t)$ and (b) group velocity $v_g(z,t)$ at the excitation point ($z = 0$; curves 1) and at the wave front ($z = t$; curve/line 2). Note that the HW group velocity at the wave front remains unchanged at the magnon velocity (v_m). In the calculation (for both 1 and 2), the damping constant of λ=0.1 is assumed. The results for the dissipationless case (λ=0) are also shown for comparison (lines 3). The insets illustrate the time domain where the values for ω_p and v_g change to negative. The thin lines at zero are provided for reference.

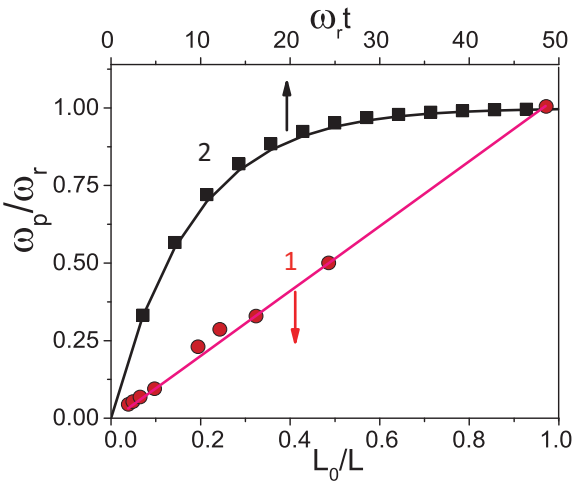

FIG. 4. Steady-state rotation frequency ω_p vs. length L of the AFM strip (line 1). L_0 denotes the size of the excitation area, where the AFM and HM layers overlap [see Fig. 1(a)]. The solid line represents the estimate based on Eq. (17), while the data points are from micro-magnetic simulations. In addition, curve 2 shows the temporal evolution of ω_p in the limiting case of $L = L_0$ based on the analytical expression [Eq. (9)] as well as the corresponding numerical calculations (data points). The micro-magnetic simulations assume the conditions of $L_0 = 20$ nm, ω_r=667 GHz, $\lambda = 0.06$, and $v_m = 6.33 \times 10^5$ cm/s. The torque is estimated by using the procedure of Ref. [7] with the current density of 3×10^7 A/cm^2.

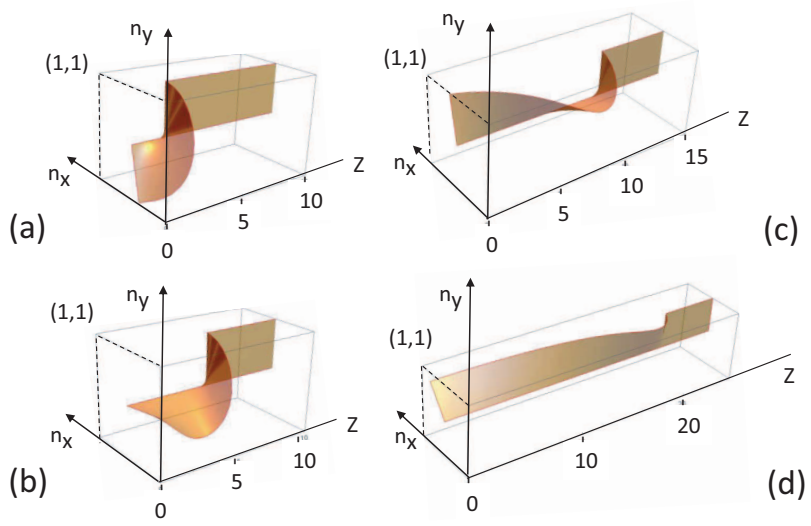

FIG. 5. Snapshots of Néel vector texture $\mathbf{n} = [n_x(z,t), n_y(z,t), 0]$ in the AFM strip under a field-like spin-pumping torque of T_q=5 at instant t=2, 5, 10, 20 for (a)-(d), respectively. The applied effective field is assumed to have a pulse-like form with the rise time of ω_r^{-1} and the relaxation time of $8\omega_r^{-1}$. The pulse duration is taken to be sufficiently long (e.g., $35\omega_r^{-1}$ in physical units). The damping constant of λ=0.1 is used for all cases (in dimensionless units).